

First-principles design of ferromagnetic monolayer MnO_2 at the complex interface

Rui-Qi Wang^{1,2}, Tian-Min Lei¹, and Yue-Wen Fang^{3,4,5*}

¹ *School of Advanced Materials and Nanotechnology,
XiDian University, Xi'an 710126, China*

² *School of Electronic Engineering,
Xi'an Aeronautical Institute, Xi'an 710077, China*

³ *Key Laboratory of Polar Materials and Devices (MOE),
Ministry of Education, Department of Electronics,
East China Normal University, Shanghai 200241, China*

⁴ *Centro de Física de Materiales (CSIC-UPV/EHU),
Manuel de Lardizabal Pasealekua 5,
20018 Donostia/San Sebastián, Spain*

⁵ *Fisika Aplikatua Saila, Gipuzkoako Ingeniaritza Eskola,
University of the Basque Country (UPV/EHU),
Europa Plaza 1, 20018 Donostia/San Sebastián, Spain*

(Dated: May 24, 2023)

Abstract

Rapidly increasing interest in low-dimensional materials is driven by the emerging requirement to develop nanoscale solid-state devices with novel functional properties that are not available in three-dimensional bulk phases. Among the well-known low-dimensional systems, complex transition metal oxide interface holds promise for broad applications in electronic and spintronics devices. Herein, intriguing metal-insulator and ferromagnetic-antiferromagnetic transitions are achieved in monolayer MnO_2 that is sandwiched into SrTiO_3 -based heterointerface systems through interface engineering. By using first-principles calculations, we modeled three types of SrTiO_3 -based heterointerface systems with different interface terminations and performed a comparative study on the spin-dependent magnetic and electronic properties that are established in the confined MnO_2 monolayer. First-principles study predicts that metal-insulator transition and magnetic transition in the monolayer MnO_2 are independent on the thickness of capping layers. Moreover, 100% spin-polarized two-dimensional electron gases accompanied by robust room temperature magnetism are uncovered in the monolayer MnO_2 . Not only is the buried MnO_2 monolayer a new interface phase of fundamental physical interest, but it is also a promising candidate material for nanoscale spintronics applications. Our study suggests interface engineering at complex oxide interfaces is an alternative approach to designing high-performance two-dimensional materials.

I. INTRODUCTION

A central goal in materials physics and materials engineering is to achieve precise control over low-dimensional materials at the atomic level with the reduction of the size of solid-state devices^{1–4}. 2D CrI_3 has a measured Curie temperature of 45 K, which has been experimentally synthesized, and stimulated the active research in 2D ferromagnetic materials⁵ because they are more suitable for the application of nanoscale devices than the traditional magnetic materials such as diluted magnetic semiconductor ZnO ⁶. For example, the ferromagnetic order persisting down to the bilayer limit, and room temperature magnetic order have been demonstrated respectively in 2D $\text{Cr}_2\text{Ge}_2\text{Te}_6$ ⁷ and monolayer VSe_2 ⁸. Very recent studies have predicted magnetic ordering in a variety of 2D materials such as CrX_3 ($\text{X} = \text{I}, \text{Br}, \text{Cl}$)⁹, NiI_2 ¹⁰, Cr_2Te_3 ¹¹, and Fe_3GeTe_2 ¹². However, only a few two-dimensional materials own robust magnetism above room temperature^{13,14}.

One alternative way to incorporate magnetism into two-dimensional materials is to synthesize transition metal oxide nanosheet. Monolayer MnO_2 is a 2D layered semiconducting transition metal oxide material that has been reliably experimentally synthesized and studied extensively with computational methods^{15–17}. Kan et al. predicted a possibly stable graphene-like antiferromagnetic MnO nanosheet and claimed single-layer doped MnO could become a half-metallic ferromagnet with Curie temperature of 350 K¹⁸. Diffusion Monte Carlo (DMC) and DFT+ U methods are used to calculate the magnetic properties of monolayer MnO_2 and find that the ferromagnetic ordering is more favorable than antiferromagnetic one¹⁹. Regardless of the difficulty in preparing free standing MnO nanosheet with graphene-like structure, some recent studies have succeeded in manufacturing transition metal oxide nanosheets. For example, we have demonstrated a direct metallic conversion from nickel hydroxide nanosheets to nickel metal nanostructures by thermal annealing in vacuum, and proved that the converted nickel metallic structures exhibit ferromagnetic behavior revealed by x-ray magnetic circular dichroism measurement²⁰. In addition, a method of wet-chemical synthesis was recommended to make two-dimensional transition metal nanosheets²¹, and this method has been applied to make $\alpha\text{-Fe}_2\text{O}_3$ —a magnetic semiconductor with intrinsic ferromagnetism at room temperature²². Very recently, a variety of studies on the synthesis of magnetic MnO_2 nanorods²³ and $\text{Fe}_3\text{O}_4/\text{MnO}_2$ nanocomposite with their applications as sorbents²⁴, catalysts²⁵, and photodegradation agents²⁶ have

been published. Moreover, MnO_2 nanoparticles and its nanocomposite with nitrogen-doped graphene have been fabricated via simple hydrothermal synthesis procedure using water as a solvent, in which the strong ferromagnetic character of nanohybrid helps in easy separation of catalyst even with a bar magnet²⁷. Nevertheless, using the above methods, defects could be introduced to two-dimensional nanosheets due to the sensitive reactions to chemical circumstances (e.g., aqueous solution), which not only makes it difficult to realize flexibly artificial control of properties of materials, but also may have a destructive effect on the spin ordering^{28,29}. A better alternative to obtain controllable couplings of lattice, charge and spin order in defect-free materials is to make use of the appealing properties of two-dimensional transition metal oxide layers sandwiched at the complex perovskite oxide interfaces. Even so, little attention has been paid to this kind of buried two-dimensional materials up till now.

Benefiting from the steady development of solid-state synthesis method (e.g., pulsed laser deposition), great success has been achieved in preparing defect-free complex oxide interfaces in the latest decade. One of the most representative instances is the transition metal complex oxide $\text{LaAlO}_3/\text{SrTiO}_3$ interface confining quasi two-dimensional electron gas (2DEG) at the nanoscale^{30,31}. Control variables have been successfully utilized to manipulate the 2DEG, such as fully optical modulation³², electronic reconstructions³³, ferroelectric polarization³⁴, electric field-effect through the gate³⁵. Surprisingly, the fascinating interface even also supports superconductivity³⁶, electronic phase separation^{37,38}, and strong Rashba spin-orbital coupling³⁹. The structure of $\text{LaAlO}_3/\text{SrTiO}_3$ interface is actually an atomic stacking sequence of perovskite structure ABO_3 . This scenario of stacking is very popular to explore interesting properties at the two-dimensional perovskite materials^{40–42}. For ferromagnet SrRuO_3 below 2-4 unit cells, ferromagnetic/metal to antiferromagnetic/insulator transitions were predicted as the result of inversion symmetry breaking combined with non-degenerate Ru $4d$ orbitals via crystal field splitting^{43–45}.

Herein, intrigued by the emergent phenomenon of stacking perovskite oxides, the aim of the present article is to theoretically design new two-dimensional transition metal oxides that can be accessible by solid-state synthesis methods. By carrying out first-principles calculations, metal-insulator transition involving antiferromagnetism-magnetism transition is observed in the monolayer MnO_2 , and 100% spin-polarized two-dimensional electron gas is extremely confined into the ferromagnetic monolayer with quite robust ferromagnetism with

at least $3.11 \mu_B/\text{Mn}$. The magnetism is predicted to remain at room/higher temperatures within mean-field theory and Heisenberg model.

II. METHOD

First-principles density functional theory calculations are all performed using the Vienna *ab initio* Simulation Package (VASP)^{46,47} along with the projector augmented wave method⁴⁸ and local density approximation (LDA). The kinetic energy cutoff of 500 eV is used for expanding the plane-wave basis set. Γ centered $7 \times 7 \times 1$ and $14 \times 14 \times 1$ Monkhorst-Pack k -meshes⁴⁹ are used for total energy calculations and densities of states calculations, respectively.

The on-site repulsion (Hubbard U) item in the approach of Dudarev et al.⁵⁰ is introduced in Hamiltonian to include approximately the effects of localized electronic correlations that are missing from standard LDA calculations. The effective Hubbard U parameters for Ti- $3d$, La- $4f$, and Mn- $3d$ orbitals are 5 eV, 11 eV and 4.5 eV, respectively. These Hubbard U values have been proved in some previous study^{17,31} to provide insightful interpretations of interface phenomena in SrTiO₃-based heterostructure systems.

In order to avoid a spurious electric field, we use symmetrical slab models for all the heterointerface structures. A vacuum spacing of at least 26 Å is used in each slab model to eliminate the interactions between repeated slabs. Our LDA+ U calculation shows the estimated equilibrium lattice constant of bulk SrTiO₃ is 3.904 Å which is very close to its experimental value of 3.905 Å. Thus, the in-plane lattice constants of the slab models in this study are all fixed at the optimized lattice constant of bulk SrTiO₃ (3.904 Å) to simulate the epitaxial growth on the SrTiO₃ substrates.

In the slab models, all coordinates of atomic positions along [001] direction perpendicular to the interfaces are fully relaxed until the forces are less than 0.01 eV/Å, meanwhile the energy convergence criterion of 10^{-6} eV is guaranteed.

III. RESULTS

A. Electrostatic field analysis

In Figure 1, we devise three MnO_2 -sandwiched heterointerfaces which are named as case 1, case 2 and case 3. In spite of the practical difficulty in preparing such complex oxide interfaces, an alternative way to accomplish this goal can be realized in two steps. More specifically, one can first grow a unit-cell of SrMnO_3 or LaMnO_3 on TiO_2 terminated SrTiO_3 substrate, and then cover the MnO_2 monolayer terminations using nonpolar SrTiO_3 or polar LaAlO_3 overlayers. By following these steps, one former study has succeeded in fabricating such complex oxide heterointerfaces through layer-by-layer growth technique¹⁷.

Bulk SrMnO_3 is composed of two formally neutral planes, i.e. SrO and Mn^{4+}O_2 planes; while bulk LaMnO_3 is constructed by $-1 \text{ Mn}^{3+}\text{O}_2$ and $+1 \text{ LaO}$ planes. The multivalent nature of Mn cations, which can exist as either Mn^{3+} or Mn^{4+} , provides a possibility to modulate the properties of MnO_2 monolayers that are confined in SrTiO_3 -based heterointerfaces. As shown in Figure 1, different interface terminations adjacent next to the MnO_2 monolayer correspond to three types of electrostatic boundary conditions. These boundary conditions dominantly control the charge reconstruction and significantly affect the atomic and electronic structures of MnO_2 monolayer.

Formation energy of interface can be used to characterize the chemical stability of the interface, which is expressed by the following formula:

$$E_{\text{Formation}} = E_{A/B/C} - E_A - E_B - E_C \quad (1)$$

where $E_{A/B/C}$, E_A , E_B and E_C refer to the total energies of the interface, and the three different bulk components. The formation energies of interfaces are $-4.44 \text{ eV/supercell}$, $-7.34 \text{ eV/supercell}$, and $-12.06 \text{ eV/supercell}$ for case 1, case 2, and case 3, respectively, suggesting the interfaces are chemically stable. It is noted that the three different interfaces have been experimentally fabricated and validated our theoretical calculations of interface stability¹⁷.

In case 1, one unit-cell of SrMnO_3 is sandwiched between the SrTiO_3 substrate and SrTiO_3 capping layers, charge reconstruction is generally not expected at the nonpolar/nonpolar/nonpolar interface. While in case 2, monolayer MnO_2 on the SrTiO_3 substrate is buried by LaO terminated LaAlO_3 overlayers. At this nonpolar/nonpolar/polar $-\text{SrO}-\text{TiO}_2/\text{SrO}-\text{MnO}_2/\text{LaO}-\text{AlO}_2-$ interface, the electric potential (V) would diverge with

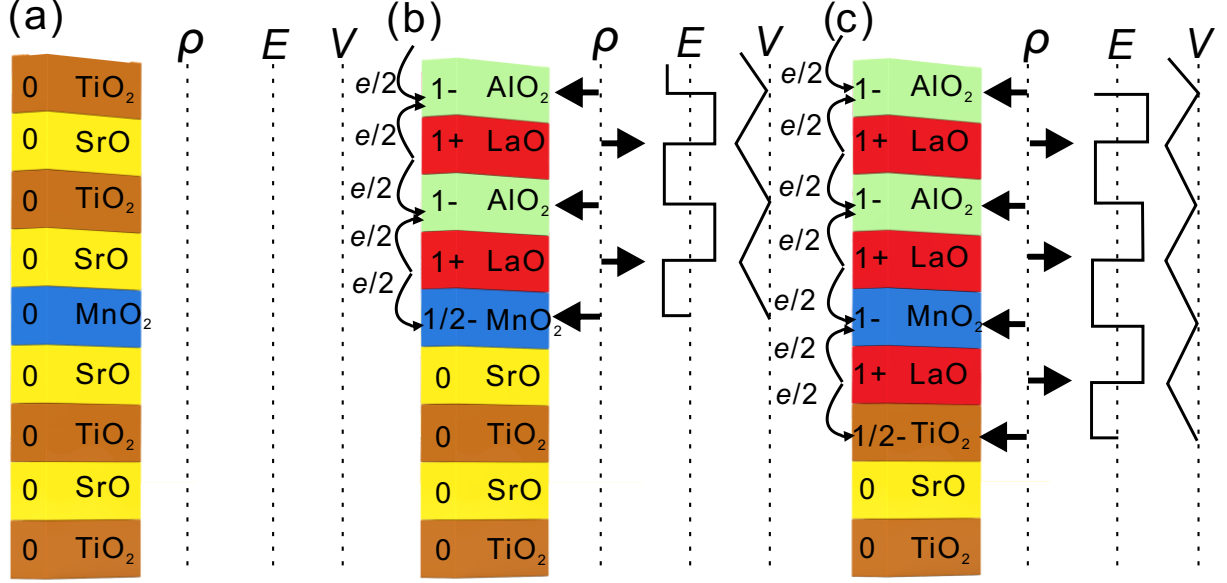


FIG. 1. (Color online) Reconstruction of electrostatic field. (a) In case 1, there is no charge transfer at the non-polar interfaces. (b) and (c) are for case 2 and case 3, respectively, in which charge transfer is expected to cause the reconstruction of the electrostatic field. In case 2, electrons transfer from one side to MnO₂ monolayer; in case 3, electrons transfer from two sides to MnO₂ monolayer.

the thickness of LaAlO₃ if there is no atomic or electronic reconstructions. This divergence catastrophe can be avoided by moving half an electron to the monolayer MnO₂ (Figure 1b). As a result, Mn is in the $(4 - x) +$ valence state ($0 < x \leq 1$). Case 3 is constructed by successively stacking three perovskites SrTiO₃, LaMnO₃, and LaAlO₃. In this structural arrangement, a nonpolar/polar/polar -SrO-TiO₂/LaO-MnO₂/LaO-AlO₂- interface is developed. Analogously to case 2, the charge at the interface is reconstructed to protect the stability of the interface from potential divergence through transferring half an electron per two-dimensional unit-cell to TiO₂ layer (Figure 1c). The corresponding valence state of Mn in this case would take the value of $(3-x) +$.

Aiming to further identify the presence of electronic reconstruction with a microscopic description, and discover the novel properties, a different method based on the principles of quantum mechanics is indispensable. First-principles calculation rooted in the framework of density-functional theory, for instance, is a tried-and-true exemplar of the successful method

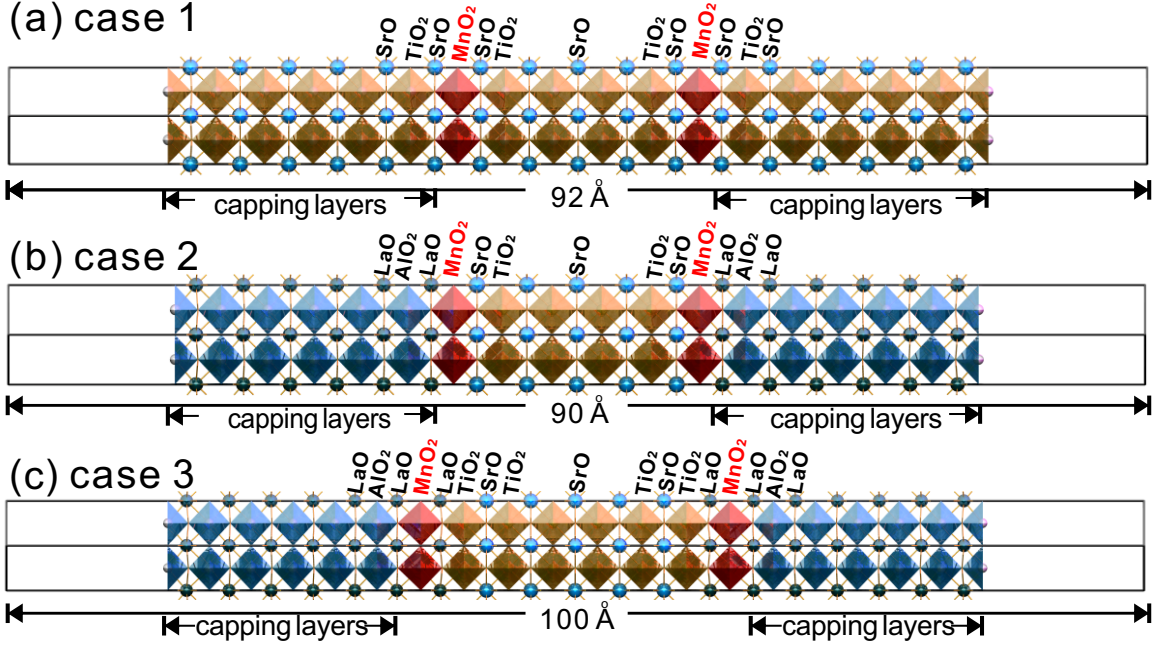


FIG. 2. (Color online) Relaxed structures of the three cases with 6 capping layers. (a) case 1. (b) case 2. (c) case 3. There is a vacuum region of at least 26 Å in each case to separate the repeated slabs.

to detect electronic and magnetic properties of materials⁵¹ and we apply it to simulate the three heterointerfaces in our study.

B. Magnetic and electronic properties

The models of the three heterointerfaces all contain two symmetrical 6 capping layers, their relaxed structures are presented in Figure 2. The alignment of spin ordering of Mn cations located in a $\sqrt{2} \times \sqrt{2} \times 1$ in-plane MnO₂ has two possible configurations, i.e. ferromagnetic or antiferromagnetic ordering. In order to get the magnetic ground state of monolayer MnO₂ in the three cases, we performed total energy calculations for each case. Table. I shows results of respective ground state, the magnetic moments of Mn, and the total magnetic moment normalized to each $\sqrt{2} \times \sqrt{2} \times 1$ in-plane MnO₂. The preferred spin configuration of monolayer MnO₂ in case 1 is antiferromagnetic ordering, while Mn-Mn exchange interactions both energetically favor ferromagnetic coupling in the other two cases. The emergent antiferromagnetic-magnetic transition in monolayer MnO₂ is interesting be-

TABLE I. Magnetic ground state, magnetic moment of Mn (μ_B/Mn) and total magnetic moment (μ_B) in the three heterointerfaces. The total magnetic moment is normalized to a $\sqrt{2} \times \sqrt{2} \times 1$ in-plane MnO_2 . AFM (FM) denotes antiferromagnetic (ferromagnetic) ground state.

Case name	Ground state	Magnetic moment/Mn (μ_B)	Total Magnetic moment (μ_B)
case 1	AFM	2.46	0
case 2	FM	3.33	6.66
case 3	FM	4.04	8.08

cause it implies that the ground state of monolayer MnO_2 can be altered by its adjoining layers, which provide new freedom to control the confined properties in monolayers. The decrease of the magnetic moments of Mn, as can be seen from the third column of Table. I, is not only the consequence of the transition of magnetic structures of monolayer MnO_2 , also indicates that the electric properties vary dramatically with the cases. Especially, there are more localized moments lying around Mn sites in case 3. We now study the electronic properties of the three cases. Figure 3(a,c,e) shows the total density of states (TDOS) of three heterointerfaces. It is clearly observed Fermi level is shifted into higher energy as the case moves from case 1 to case 2 to case 3. This shifting indicates that more electronic states are transferred into monolayer MnO_2 . Case 1 is an insulator with a narrow band gap, its insulating state verifies electronic reconstruction does not occur at the interface. On the contrary, bands crossing the Fermi level at the interfaces prove the existence of electronic reconstruction in case 2 and 3. These results are in good agreement with the results analyzed from the polar catastrophe model in Figure 1. Apart from the system properties of the whole heterointerfaces, more inviting properties are only confined in the monolayer MnO_2 . As described by the MnO_2 layer projected density of states (PDOS) in Figure 3(b,d,f), the majority and minority spin electrons make equal contributions to the layer PDOS with a band gap ~ 0.2 eV in both spin channels, resulting from the antiferromagnetic ground state in case 1. This feature of MnO_2 is similar to its parent phase. The band gap of SrMnO_3 is only ~ 0.15 eV if G-type antiferromagnetic structure is imposed on it based on our calculations. Whereas the layer PDOSs of the remaining cases are dramatically different from

that in the former case. More specifically, a highly confined 100% spin-polarized 2DEG is formed in monolayer MnO_2 in both case 2 and case 3, with a minority spin band gap ~ 1.8 eV for case 2 and ~ 0.8 eV for case 3, respectively. That is to say, metal-insulator transition in monolayer MnO_2 is realized with the accompanying of transformation of ground states.

A deeper understanding of the metal-insulator transition in MnO_2 can be gained by studying the orbital resolved PDOS. Because the models we use all contain two symmetric $\sqrt{2} \times \sqrt{2} \times 1$ in-plane MnO_2 atomic layers, each model contains four Mn atoms that can be divided into two equivalent groups according to the mirror symmetry of the structure. There are two atoms in each group, we will label them as Mn-1 and Mn-2. Figure 4 demonstrates the PDOS of Mn-1 and Mn-2 in each case. Locating in the octahedral crystal field framed by the oxygen ligands, the Mn 3d orbitals split into triplet t_{2g} -like (d_{xy} , d_{yz} , d_{xz}) and doublet e_g -like ($d_{x^2-y^2}$, $d_{z^2-r^2}$) states to lower the energy. In case 1, Mn-1 and Mn-2 contribute equally to PDOS, but in different spin channels due to the antiferromagnetic coupling between Mn-1 and Mn-2. It is the hybridizations of d_{xy} with a gain of the strongest energy lowering and O 2p states that determine the band gap (~ 0.2 eV) of MnO_2 . From -2 to 0 eV, the PDOS is mainly composed of $d_{x^2-y^2}$, d_{yz} and d_{xz} states. More importantly, the magnetism of Mn in case 1 is mostly derived from the spin splitting of these states. The majority part of d_{xy} and $d_{z^2-r^2}$ states lie in much deeper energy and show relatively smaller spin splitting. In case 2 or 3, with parallel spin ordering, Mn-1 and Mn-2 are equivalent in symmetry, hence PDOS of Mn-1 is exactly the same to that of Mn-2. The PDOS of Mn-1 in case 2 depicted in Figure 4c displays a metallic majority spin channel and a ~ 1.8 eV band gap in the minority spin channel. PDOS of Mn-1 (Figure 4e) in case 3 also shows 100% spin-polarization, but the minority spin band gap is reduced to 0.8 eV. The decrease of the band gap in the minority spin channel is caused by the energy shift of d_{yz}/d_{xz} and $d_{x^2-y^2}$ from case 2 to case 3. It is noticeable that d_{xy} and $d_{z^2-r^2}$ states are lying in lowering energy ranges in cases 2 and 3, compared to those in case 1. What is more, d_{xy} and $d_{z^2-r^2}$ states are responsible for the metallicity in the majority spin channel in case 3, the respective PDOS of them at the Fermi level are ~ 0.25 and ~ 0.125 states/eV; while in case 2, PDOS at the Fermi level is crucially dominated by d_{xy} states (~ 0.25 states/eV at the Fermi level). This discrepancy implies a much strong electronic reconstruction in case 3 because of the presence of sandwich-like -LaO- MnO_2 -LaO interface as mentioned in the previous part. Hence, we turn to study the charge state of Mn cation in each case, although qualitative results have been predicted in

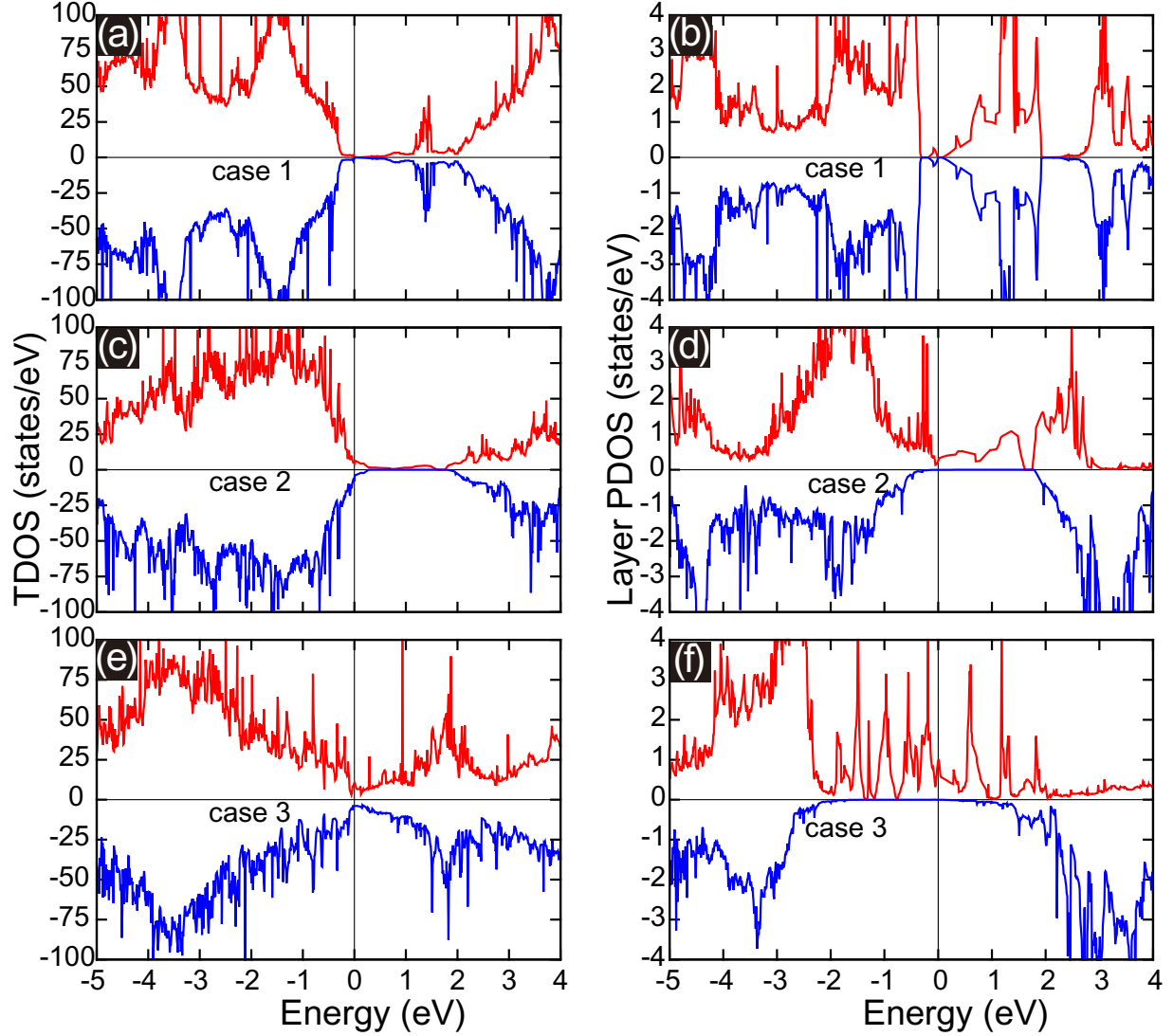


FIG. 3. (Color online) Total density of states (TDOS) of case- N ($N = 1, 2, 3$) in the left panel and the corresponding MnO_2 layer projected density of states (PDOS) in the right panel. (a) TDOS of case 1. (b) Layer PDOS of MnO_2 in case 1. (c) TDOS of case 2. (d) Layer PDOS of MnO_2 in case 2. (e) TDOS of case 3. (f) Layer PDOS of MnO_2 in case 3. 0 eV is the reference for the Fermi level.

section III A. A quantitative method to investigate the charge transfer is indispensable to gain a lucid understanding of the charge state of Mn cation. In general, such a quantitative prediction of charge state in large models containing about 200 atoms in first-principles calculations is usually not easy and time-consuming. Here, we adopt a grid-based Bader

analysis algorithm⁵² to study the charge density of specific transition metal atoms. The calculated Bader charge of Mn cation in each case is 5.0, 5.3, and 5.46, respectively. The increase of Bader charge indicates that Mn cation in case 2 (case 3) gains 0.3 (0.46) more electrons than that in case 1. Another quantitative way is also used to confirm this result. By integrating the orbital resolved PDOS to the Fermi energy, we find that valence electrons of Mn cation in case 2 has 0.15 electron less than that of case 3, and 0.21 electron more than that of case 1. One can see the results derived from these two methods are consistent.

C. Effects of the thickness of capping layers

In the above parts, we have reported a systematic study of magnetic and electronic properties for the three heterointerfaces with six capping layers. However, there remain two questions driving this study to move forward. How does the thickness of capping layers affect the ground state of monolayer MnO_2 in case 2 and 3? Does the spin-polarized 2DEG have a critical thickness as that in (001) and (100) $\text{LaAlO}_3/\text{SrTiO}_3$ interfaces^{53,54}? To answer these two questions, we investigate the effect of the thickness of capping layers on the electronic and magnetic properties of monolayer MnO_2 . Because spin-polarized 2DEG only exists in case 2 and case 3, we only address the issues for these two cases with LaAlO_3 capping layers.

case 2 and case 3 with different capping layers ($N = 1, 2, 3, 4, 6$). As can be seen, both case 2 and case 3 are stabilized in ferromagnetic ground states. It manifests thickness of capping layers does not affect the ground states in the two cases. To estimate the Curie temperature, we further performed Monte Carlo simulations using the VAMPIRE code⁵⁵ to predict the Curie temperature of the MnO_2 monolayer quantitatively. The Monte Carlo algorithm for classical spin models developed by Hinze and Nowak was used⁵⁶. We employed a large enough thin film model with a total length of 20 nm along x and y directions in the Monte Carlo simulations. The simulations begin at 0 K and end at 2000 K with a temperature increment of 1 K. The equilibration time steps and loop time steps in VAMPIRE calculations are both set to 50000 to guarantee the equilibration of each step. Figure 5 shows the normalized magnetization as a function of temperature T from the Monte Carlo simulations. The Curie temperature T_C is estimated by fitting the data in Figure 5 with the Curie-Bloch equation in the classical limit given by $M(T) = (1 - \frac{T}{T_C})^{\beta_{45}}$.

Our results also show, notwithstanding ferromagnetic ground states in these MnO_2 mono-

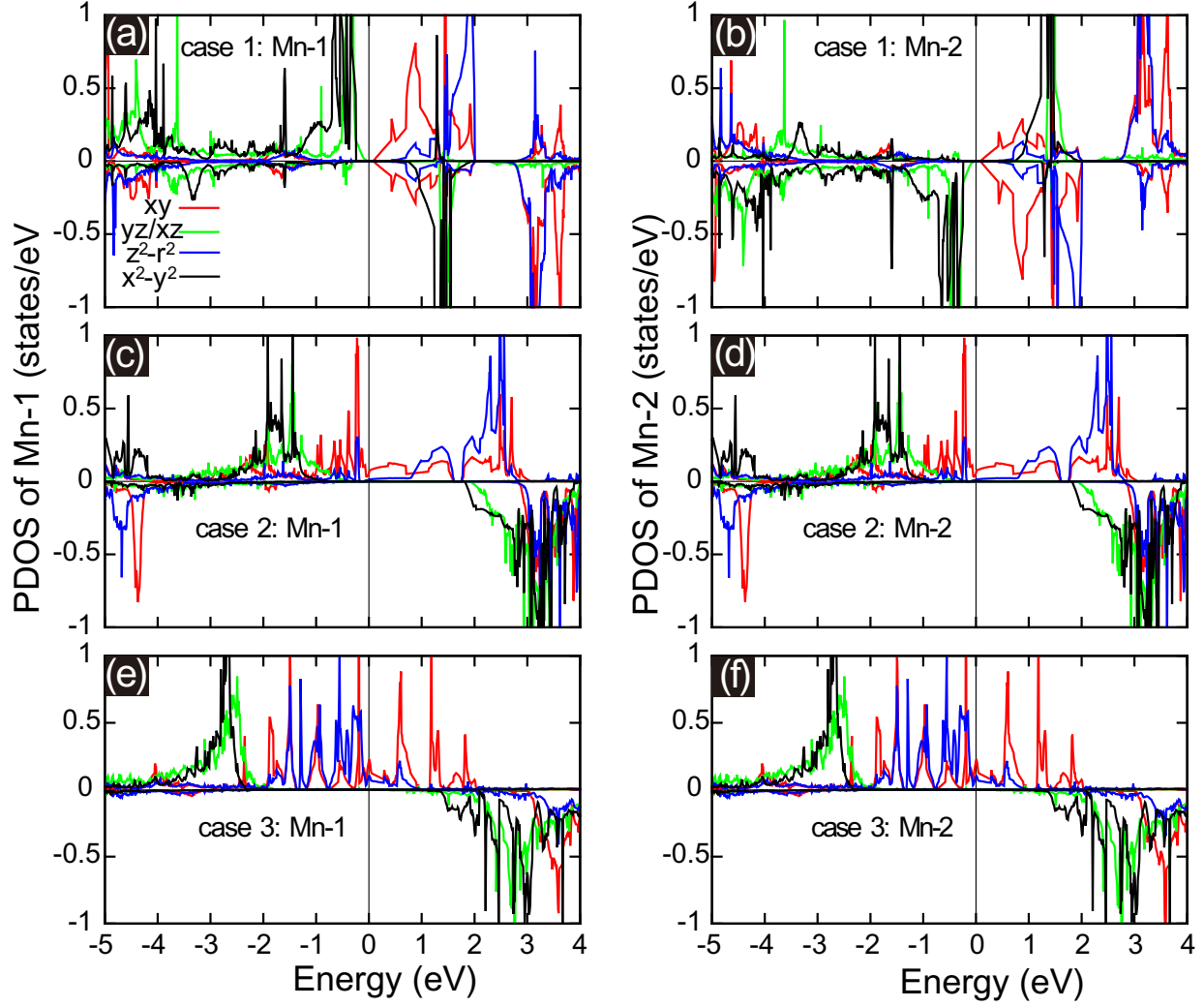


FIG. 4. (Color online) PDOS of Mn-1 and Mn-2 in case- M ($M = 1, 2, 3$) with spin and orbital resolution. (a) PDOS of Mn-1 in case 1. (b) PDOS of Mn-2 in case 1. (c) PDOS of Mn-1 in case 2. (d) PDOS of Mn-2 in case 2. (e) PDOS of Mn-1 in case 3. (f) PDOS of Mn-2 in case 3. d_{xy} , d_{yz}/d_{xz} , $d_{z^2-r^2}$, and $d_{x^2-y^2}$ are plotted by red, yellow, blue, and black solid curves, respectively. 0 eV is the reference for the Fermi level.

layers are energetically favored, magnetic moments of Mn cation show thickness-dependent behaviors. Specifically, the magnetic moment of Mn cation in case 2 decreases when LaAlO_3 layers become thinner; the situation in case 3 is a bit different, as LaAlO_3 thickness drops from $N = 6$ to $N = 2$, the magnetic moment of Mn cation is decreased from $4.04 \mu_B$ for $N = 6$ to $3.78 \mu_B$ for $N = 2$, yet there is a modest increase if one more capping layer is

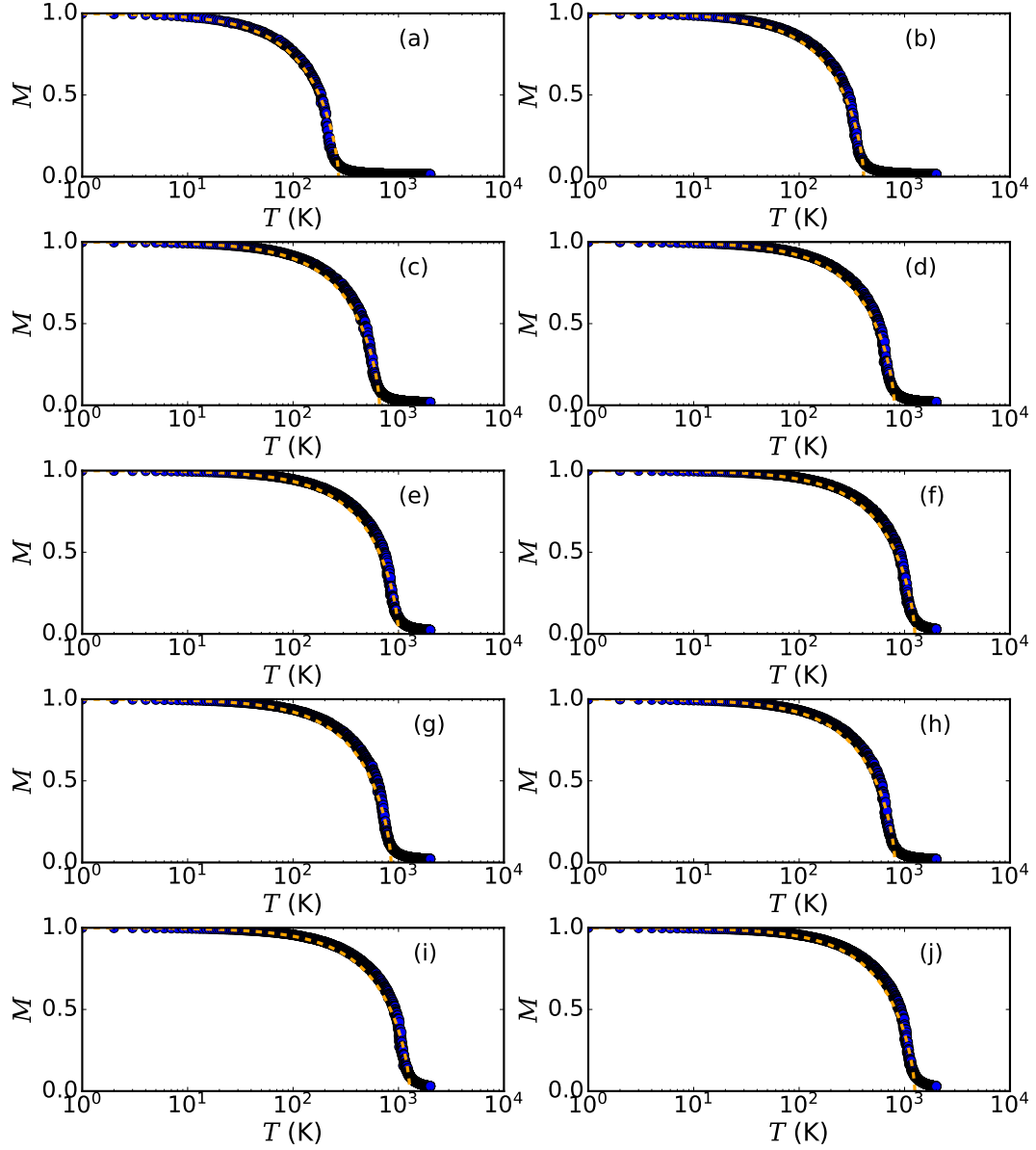


FIG. 5. (Color online) The normalized magnetization M as a function of temperature T (K). Note that the axis of temperature uses logarithmic scale. (a-e) correspond to case 2 in which capping layers $N = 1, 2, 3, 4, 6$. (f-j) correspond to case 3 in which capping layers $N = 1, 2, 3, 4, 6$. The circles are data from the Monte Carlo simulations, and the orange dashed lines are fitted from Curie-Bloch equation. The Monte Carlo simulations are simulated from 0 to 2000 K.

removed (i.e. $N = 1$), the magnetic moment becomes $3.86 \mu_B$.

TABLE II. The magnetic ground state, magnetic moment of Mn (μ_B), and calculated Curie temperature from Monte Carlo simulations for case 2 and case 3 with varying thicknesses of capping layers. FM denotes the ferromagnetic ground state.

Case name	Capping layers	Ground state	Magnetic moment/Mn (μ_B)	T_c (K)
case 2	6	FM	3.33	1000
case 2	4	FM	3.32	810
case 2	3	FM	3.20	660
case 2	2	FM	3.18	410
case 2	1	FM	3.11	270
case 3	6	FM	4.04	1250
case 3	4	FM	4.01	1280
case 3	3	FM	3.83	810
case 3	2	FM	3.78	850
case 3	1	FM	3.86	1250

Electronic properties. Figure 6 displays the MnO_2 layer PDOS in case 2 and case 3 with thickness dependence. Except for the abrupt decline in spin polarization ($\sim 23.0\%$) of MnO_2 in case 2 with $N = 2$, the remaining MnO_2 layers all show well-defined half-metallicity. For special case 2 with two capping layers, we find the orbital occupation of O p_z in the minority spin channel is responsible for the remarkable reduction of spin polarization of monolayer MnO_2 . Furthermore, the exchange splitting of O p_z introduces $\sim 0.05 \mu_B$ local moments at the sites of oxygen.

Structure interpretation. In order to build a relationship between the structure and the above observations qualitatively. We examined the Mn-O(1)/Mn-O(2) bond length and Mn-O displacements perpendicular to the plane of the MnO_2 monolayer. The left panel of Figure 7 presents Mn-O(1)/Mn-O(2) bond length as a function of the thickness of capping layers.

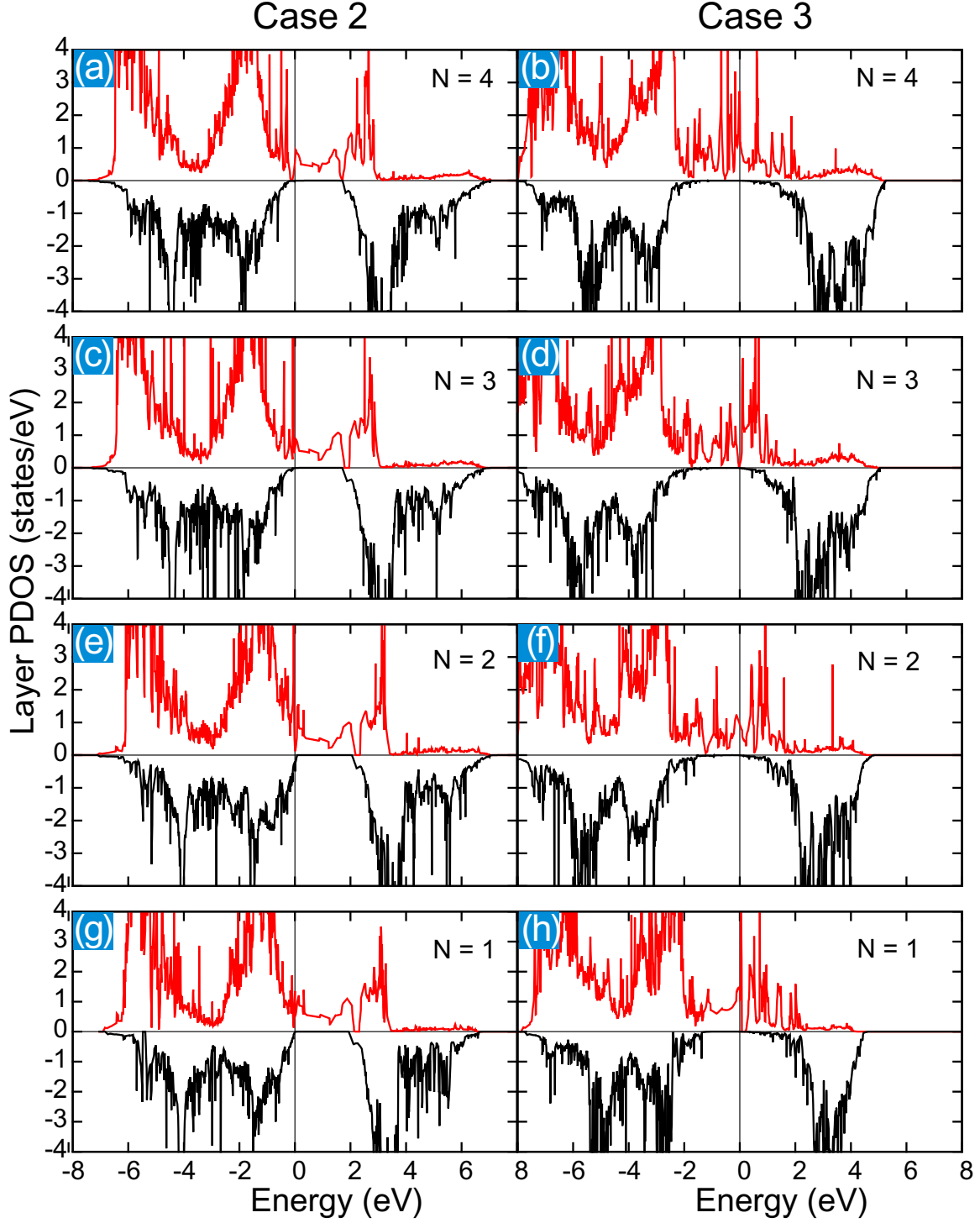


FIG. 6. (Color online) MnO₂ layer projected PDOS. Left panel: PDOS of case 2 with N capping layers [$N = 4$ (a), 3 (c), 2(e), and 1(g)]. Right panel: PDOS of case 3 with N capping layers [$N = 4$ (b), 3 (d), 2(f), and 1(h)]. 0 eV is the reference for the Fermi level. Red and black solid curves denote majority and minority spin channels, respectively

We note that the bond length of Mn-O(1)/Mn-O(2) in case 2 is decreased with the decreasing thickness, whose trend is the same as that of the magnetic moment of Mn ions in this case. In case 3, the bond length of Mn-O is decreased with the reducing capping layers when $N \geq 2$, but it is increased when $N = 1$, this result coincides to the trend of magnetic moment in case 3. Therefore, the magnetic moments of Mn cations are fundamentally associated with the bond length of Mn-O. In the right panel of Figure 7, we also analyze the Mn-O displacements so as to interpret the introduced $0.05 \mu_B$ magnetic moment at the oxygen site. By surveying all the data in the right panel, it is found the Mn-O displacement in case 2 with $N = 2$ is the smallest ($\sim 0.025 \text{ \AA}$) among all the calculated structures, in this situation, Mn-O covalency bonding is stronger than other structures by hybridizing Mn-3d with O-2p orbitals.

IV. DISCUSSION

By designing three heterointerfaces with varying thicknesses of capping layers, metal-insulator transition, as well as the magnetic transition was revealed in monolayer MnO_2 by analyzing the electronic and magnetic properties. The metal-insulator transition and ferromagnetic-antiferromagnetic transition are independent on the thickness of the capping layers but are linked to the adjoining layers that determine the occurrence of electronic reconstruction. The vanishing critical thickness of the 100% spin-polarized 2DEG is very different from that in $\text{LaAlO}_3/\text{SrTiO}_3$ with the critical thickness of three layers⁵⁷. We think this discrepancy is chiefly ascribed to the band gap of monolayer MnO_2 and in-built electric field in the capping layers. The band gap of monolayer MnO_2 is only about 0.2 eV in calculations, which can be easily destroyed by the sizable internal electric field $\sim 0.24 \text{ V/\AA}$ in a unit-cell LaAlO_3 ⁵⁸. As a result, critical thickness vanishes.

Our current findings show the magnetic transition is closely correlated to the metal-insulator transition. In case 1, we find the 180° Mn-O-Mn bond is well preserved. Being an insulator containing $t_{2g}^3 e_g^0$ magnetic ions, its spin ordering can be understood by the Goodenough-Kanamori-Anderson (GKA) rules⁵⁹. A 180° Mn-O-Mn bond can give rise to antiferromagnetic superexchange by hopping between two half-filled active orbitals and the same ligand p orbital (i.e. $pd\pi$ hopping in this case)⁶⁰. Differing from case 1, case 2 and case 3 display spin-polarized conductivity. In these two systems, the magnetic interactions

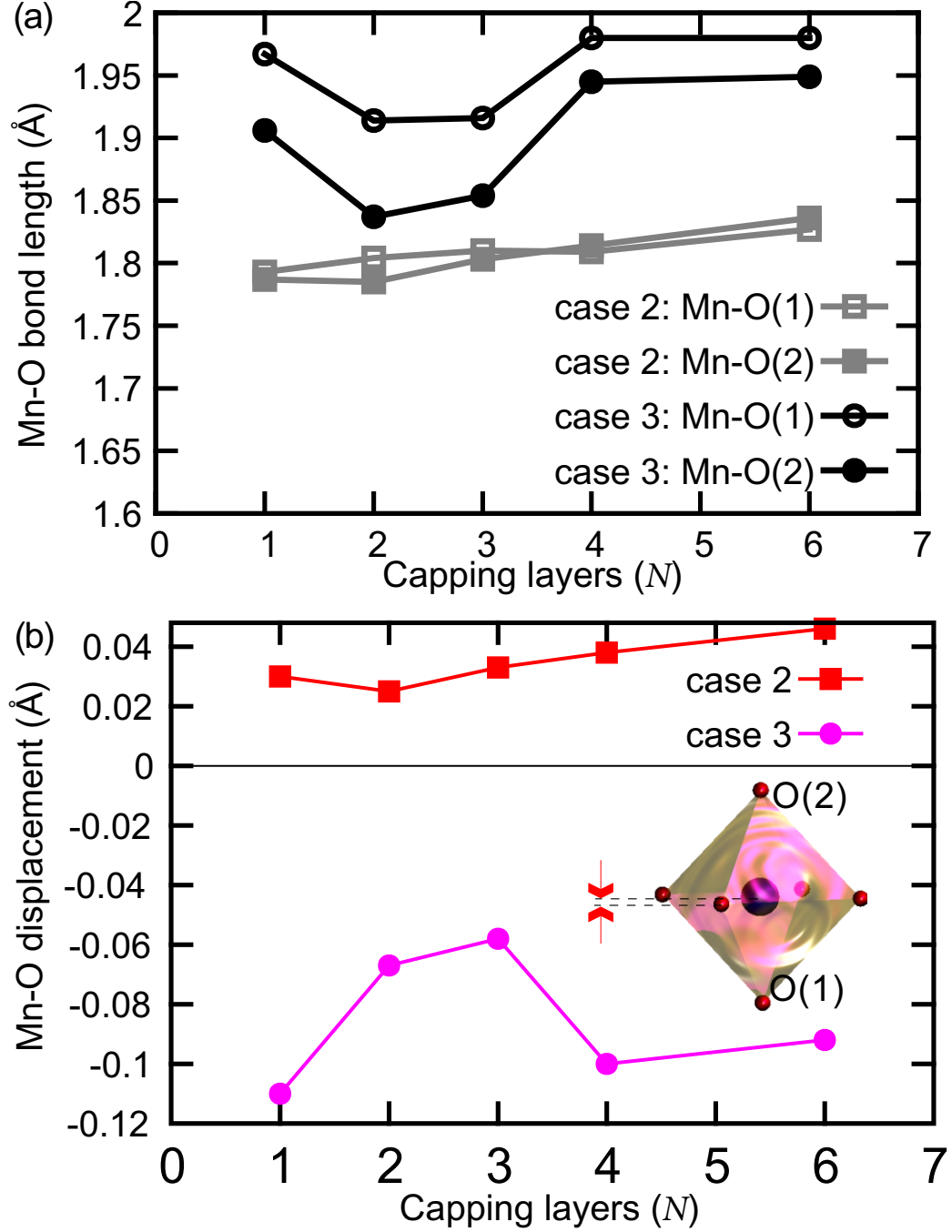


FIG. 7. (Color online) Mn-O displacement and Mn-O bond length against the thickness of capping layers. (a) The bond lengths of Mn-O(1) and Mn-O(2) as the function of the thickness of capping layers. Here, we assign O(1) in the substrate and O(2) in the capping layer. (b) Mn-O displacements (Å) along z -direction as the function of the thickness of capping layers. The spacing indicated by the two red arrows illustrates the Mn-O displacement in the octahedral MnO₆ cage. Positive (negative) sign in the displacement axis means z_{Mn} is bigger (smaller) than z_{O}

are dominated by the coupling between the localized and itinerant electrons. This exchange, also known as double exchange or Zener exchange⁶¹, leads to the ferromagnetic coupling, and has also been reported to stabilize the ferromagnetic order in the $(\text{LaMnO}_3)_n/(\text{SrTiO}_3)_m$ superlattices⁶² and $\text{LaMnO}_3/\text{SrTiO}_3$ heterostructures with hole or electron doping⁴² recently.

V. CONCLUSION

In summary, monolayer MnO_2 is designed to be sandwiched at complex oxide heterointerfaces, their electronic and magnetic structures with varying thicknesses of capping layers are systematically investigated by the first-principles calculations. Due to the presence of charge reconstruction at the interface, metal-insulator transition and magnetic transition are both observed in the one-atom-thick MnO_2 . Our results show these transitions are independent of the thickness, which makes it stand out from (001) and (110) $\text{LaAlO}_3/\text{SrTiO}_3$ with critical thickness. In addition, 100% spin-polarized 2DEG with robust room-temperature ferromagnetism are reported in the buried monolayer MnO_2 , we predict it can potentially be applied to the next-generation nanoscale spintronic devices. This work presents fascinating phenomena in monolayer transition metal with first-principles calculations and paves an innovative way to design novel two-dimensional materials. We expect the present study will motivate more efforts to study the two-dimensional transition metal oxides and their future applications in various electronic/spintronic devices.

ACKNOWLEDGEMENTS

The authors R.-Q.W. and Y.-W.F. acknowledge the discussions with Chun-Gang Duan during their stay at East China Normal University (ECNU). Y.-W.F. thanks the support from his current laboratory led by Ion Errea for the great support on the research activities. The computations were primarily performed by Y.-W.F. at the High-Performance Computing Center of ECNU, with minor contributions from R.-Q.W. who is supported by the Scientific Research Program Funded by Shaanxi Provincial Education Department (Program No.21JK0699) and School level fund of Xi'an Aeronautical Institute (Program No.2020KY1224). Y.-W.F. supervised and investigated this project, and wrote the manuscript during his stay at ECNU. R.-Q.W. improved the manuscript by rewriting the

introduction, interpreting and appending computational results on interface stability with T.-M.L.’s assistance. All authors have contributed to reviewing the manuscript.

DECLARATION OF COMPETING INTEREST

The authors declare no competing interests.

DATA AVAILABILITY

All data that support the findings of this study are included in the article, and the freely open database Zenodo⁶³.

* fyuewen@gmail.com

- ¹ Q. Yang, J. Hu, Y.-W. Fang, Y. Jia, R. Yang, S. Deng, Y. Lu, O. Dieguez, L. Fan, D. Zheng, X. Zhang, Y. Dong, Z. Luo, Z. Wang, H. Wang, M. Sui, X. Xing, J. Chen, J. Tian, and L. Zhang, *Science* **379**, 1218 (2023).
- ² Y. Wu, J. Li, and Y. Liu, *J. Phys.: Condens. Matter* **35**, 083002 (2022).
- ³ X.-W. Shen, Y.-W. Fang, B.-B. Tian, and C.-G. Duan, *ACS Appl. Electron. Mater.* **1**, 1133 (2019).
- ⁴ W.-Y. Tong, Y.-W. Fang, J. Cai, S.-J. Gong, and C.-G. Duan, *Computational Materials Science* **112**, 467 (2016).
- ⁵ B. Huang, G. Clark, E. Navarro-Moratalla, D. R. Klein, R. Cheng, K. L. Seyler, D. Zhong, E. Schmidgall, M. A. McGuire, D. H. Cobden, W. Yao, D. Xiao, P. Jarillo-Herrero, and X. Xu, *Nature* **546**, 270 (2017).
- ⁶ T. A. Abdel-Baset, Y.-W. Fang, C.-G. Duan, and M. Abdel-Hafiez, *J Supercond Nov Magn* **29**, 1937 (2016).
- ⁷ C. Gong, L. Li, Z. Li, H. Ji, A. Stern, Y. Xia, T. Cao, W. Bao, C. Wang, Y. Wang, Z. Q. Qiu, R. J. Cava, S. G. Louie, J. Xia, and X. Zhang, *Nature* **546**, 265 (2017).
- ⁸ M. Bonilla, S. Kolekar, Y. Ma, H. C. Diaz, V. Kalappattil, R. Das, T. Eggers, H. R. Gutierrez, M.-H. Phan, and M. Batzill, *Nature Nanotech* **13**, 289 (2018).

- ⁹ L. Liu, Z. Lin, J. Hu, and X. Zhang, *Nanoscale* **13**, 8137 (2021).
- ¹⁰ Q. Song, C. A. Occhialini, E. Ergeçen, B. Ilyas, D. Amoroso, P. Barone, J. Kapeghian, K. Watanabe, T. Taniguchi, A. S. Botana, S. Picozzi, N. Gedik, and R. Comin, *Nature* **602**, 601 (2022).
- ¹¹ J. Zhong, M. Wang, T. Liu, Y. Zhao, X. Xu, S. Zhou, J. Han, L. Gan, and T. Zhai, *Nano Res.* **15**, 1254 (2022).
- ¹² Z. Fei, B. Huang, P. Malinowski, W. Wang, T. Song, J. Sanchez, W. Yao, D. Xiao, X. Zhu, A. F. May, W. Wu, D. H. Cobden, J.-H. Chu, and X. Xu, *Nature Mater* **17**, 778 (2018).
- ¹³ G. Song, D. Li, H. Zhou, C. Zhang, Z. Li, G. Li, B. Zhang, X. Huang, and B. Gao, *Appl. Phys. Lett.* **118**, 123102 (2021).
- ¹⁴ X. Zhang, Q. Lu, W. Liu, W. Niu, J. Sun, J. Cook, M. Vaninger, P. F. Miceli, D. J. Singh, S.-W. Lian, T.-R. Chang, X. He, J. Du, L. He, R. Zhang, G. Bian, and Y. Xu, *Nat Commun* **12**, 1133 (2021).
- ¹⁵ D. A. Kitchaev, H. Peng, Y. Liu, J. Sun, J. P. Perdew, and G. Ceder, *Phys. Rev. B* **93**, 045132 (2016).
- ¹⁶ S. Rong, P. Zhang, and F. Liu, *J. Phys.: Condens. Matter* **32**, 015301 (2020).
- ¹⁷ H.-J. Liu, J.-C. Lin, Y.-W. Fang, J.-C. Wang, B.-C. Huang, X. Gao, R. Huang, P. R. Dean, P. D. Hatton, Y.-Y. Chin, H.-J. Lin, C.-T. Chen, Y. Ikuhara, Y.-P. Chiu, C.-S. Chang, C.-G. Duan, Q. He, and Y.-H. Chu, *Adv. Mater.* **28**, 9142 (2016).
- ¹⁸ E. Kan, M. Li, S. Hu, C. Xiao, H. Xiang, and K. Deng, *J. Phys. Chem. Lett.* **4**, 1120 (2013).
- ¹⁹ D. Wines, K. Saritas, and C. Ataca, *J. Phys. Chem. C* **126**, 5813 (2022).
- ²⁰ Y. Naruo, S. Uechi, M. Sawada, A. Funatsu, F. Shimojo, S. Ida, and M. Hara, *Nanotechnology* **31**, 435602 (2020).
- ²¹ C. Tan and H. Zhang, *Nat Commun* **6**, 666 (2015).
- ²² W. Cheng, J. He, T. Yao, Z. Sun, Y. Jiang, Q. Liu, S. Jiang, F. Hu, Z. Xie, B. He, W. Yan, and S. Wei, *J. Am. Chem. Soc.* **136**, 10393 (2014).
- ²³ D. Gangwar and C. Rath, *Applied Surface Science* **557**, 149693 (2021).
- ²⁴ S. Chen and F. Xie, *Applied Surface Science* **507**, 145090 (2020).
- ²⁵ Z. Bakhtiarzadeh, S. Rouhani, Z. Karimi, S. Rostamnia, T. A. Msagati, D. Kim, H. W. Jang, S. Ramakrishna, R. S. Varma, and M. Shokouhimehr, *Molecular Catalysis* **509**, 111603 (2021).
- ²⁶ M. Dubey, N. V. Challagulla, S. Wadhwa, and R. Kumar, *Colloids and Surfaces A: Physico-chemical and Engineering Aspects* **609**, 125720 (2021).

- ²⁷ R. Singh, M. Kumar, L. Tashi, H. Khajuria, and H. N. Sheikh, *Molecular Physics* **117**, 2477 (2019).
- ²⁸ M. A. Awad and N. M. A. Hadia, *J Mater Sci: Mater Electron* **29**, 20695 (2018).
- ²⁹ S. I. Shah, Zulfiqar, T. Khan, R. Khan, S. A. Khan, S. A. Khattak, and G. Khan, *J Mater Sci: Mater Electron* **30**, 19199 (2019).
- ³⁰ Y.-L. Han, Y.-W. Fang, Z.-Z. Yang, C.-J. Li, L. He, S.-C. Shen, Z.-Z. Luo, G.-L. Qu, C.-M. Xiong, R.-F. Dou, X. Wei, L. Gu, C.-G. Duan, and J.-C. Nie, *Phys. Rev. B* **92**, 115304 (2015).
- ³¹ F. Zhang, Y.-W. Fang, N. Y. Chan, W. C. Lo, D. F. Li, C.-G. Duan, F. Ding, and J. Y. Dai, *Phys. Rev. B* **93**, 214427 (2016).
- ³² W. Niu, Y.-W. Fang, R. Liu, Z. Wu, Y. Chen, Y. Gan, X. Zhang, C. Zhu, L. Wang, Y. Xu, Y. Pu, Y. Chen, and X. Wang, *J. Phys. Chem. Lett.* **13**, 2976 (2022).
- ³³ W. Niu, Y. Fang, X. Zhang, Y. Weng, Y. Chen, H. Zhang, Y. Gan, X. Yuan, S. Zhang, J. Sun, Y. Wang, L. Wei, Y. Xu, X. Wang, W. Liu, and Y. Pu, *Adv. Electron. Mater.* **7**, 2000803 (2021).
- ³⁴ P. Sharma, S. Ryu, Z. Viskadourakis, T. R. Paudel, H. Lee, C. Panagopoulos, E. Y. Tsymbal, C.-B. Eom, and A. Gruverman, *Adv. Funct. Mater.* **25**, 6538 (2015).
- ³⁵ A. M. R. V. L. Monteiro, D. J. Groenendijk, N. Manca, E. Mulazimoglu, S. Goswami, Y. Blanter, L. M. K. Vandersypen, and A. D. Caviglia, *Nano Lett.* **17**, 715 (2017).
- ³⁶ Y.-L. Han, S.-C. Shen, J. You, H.-O. Li, Z.-Z. Luo, C.-J. Li, G.-L. Qu, C.-M. Xiong, R.-F. Dou, L. He, D. Naugle, G.-P. Guo, and J.-C. Nie, *Appl. Phys. Lett.* **105**, 192603 (2014).
- ³⁷ Ariando, X. Wang, G. Baskaran, Z. Q. Liu, J. Huijben, J. B. Yi, A. Annadi, A. R. Barman, A. Rusydi, S. Dhar, Y. P. Feng, J. Ding, H. Hilgenkamp, and T. Venkatesan, *Nat Commun* **2**, 1 (2011).
- ³⁸ N. Scopigno, D. Bucheli, S. Caprara, J. Biscaras, N. Bergeal, J. Lesueur, and M. Grilli, *Phys. Rev. Lett.* **116**, 026804 (2016).
- ³⁹ G. Herranz, G. Singh, N. Bergeal, A. Jouan, J. Lesueur, J. Gázquez, M. Varela, M. Scigaj, N. Dix, F. Sánchez, and J. Fontcuberta, *Nat Commun* **6**, 9904 (2015).
- ⁴⁰ B. Yin, P. Aguado-Puente, S. Qu, and E. Artacho, *Phys. Rev. B* **92**, 115406 (2015).
- ⁴¹ D. W. Jeong, W. S. Choi, S. Okamoto, J.-Y. Kim, K. W. Kim, S. J. Moon, D.-Y. Cho, H. N. Lee, and T. W. Noh, *Sci Rep* **4**, 1039 (2015).

- ⁴² X. R. Wang, C. J. Li, W. M. Lü, T. R. Paudel, D. P. Leusink, M. Hoek, N. Poccia, A. Vailionis, T. Venkatesan, J. M. D. Coey, E. Y. Tsymbal, Ariando, and H. Hilgenkamp, *Science* **349**, 716 (2015).
- ⁴³ Y. J. Chang, C. H. Kim, S. H. Phark, Y. S. Kim, J. Yu, and T. W. Noh, *Phys. Rev. Lett.* **103**, 057201 (2009).
- ⁴⁴ A. Huang, S.-H. Hung, and H.-T. Jeng, *Applied Sciences* **8**, 2151 (2018).
- ⁴⁵ H.-J. Liu, M. Ye, C.-Y. Yang, Y.-W. Fang, Y.-Y. Chin, C.-Y. Chen, R. T. Hung, Y. Zhu, L.-C. He, M.-Y. Huang, L. Chen, M. Gu, S. Ke, Y.-F. Liao, K.-D. Tsuei, H.-J. Lin, C.-T. Chen, S. Agrestini, J. Herrero-Martin, and C.-H. Lai, *Applied Materials Today* **24**, 101101 (2021).
- ⁴⁶ G. Kresse and J. Furthmüller, *Computational Materials Science* **6**, 15 (1996).
- ⁴⁷ G. Kresse and J. Furthmüller, *Phys. Rev. B* **54**, 11169 (1996).
- ⁴⁸ P. E. Blöchl, *Phys. Rev. B* **50**, 17953 (1994).
- ⁴⁹ H. J. Monkhorst and J. D. Pack, *Phys. Rev. B* **13**, 5188 (1976).
- ⁵⁰ S. L. Dudarev, G. A. Botton, S. Y. Savrasov, C. J. Humphreys, and A. P. Sutton, *Phys. Rev. B* **57**, 1505 (1998).
- ⁵¹ Y.-W. Fang, H.-C. Ding, W.-Y. Tong, W.-J. Zhu, X. Shen, S.-J. Gong, X.-G. Wan, and C.-G. Duan, *Science Bulletin* **60**, 156 (2015).
- ⁵² G. Henkelman, A. Arnaldsson, and H. Jónsson, *Computational Materials Science* **36**, 354 (2006).
- ⁵³ S. Thiel, G. Hammerl, A. Schmehl, C. W. Schneider, and J. Mannhart, *Science* **313**, 1942 (2006).
- ⁵⁴ A. Annadi, Q. Zhang, X. Renshaw Wang, N. Tuzla, K. Gopinadhan, W. M. Lü, A. Roy Barman, Z. Q. Liu, A. Srivastava, S. Saha, Y. L. Zhao, S. W. Zeng, S. Dhar, E. Olsson, B. Gu, S. Yunoki, S. Maekawa, H. Hilgenkamp, T. Venkatesan, and Ariando, *Nat Commun* **4**, 103 (2013).
- ⁵⁵ R. F. L. Evans, W. J. Fan, P. Chureemart, T. A. Ostler, M. O. A. Ellis, and R. W. Chantrel, *J. Phys. Condens. Matter* **26**, 103202 (2014).
- ⁵⁶ P. Asselin, R. F. L. Evans, J. Barker, R. W. Chantrell, R. Yanes, O. Chubykalo-Fesenko, D. Hinzke, and U. Nowak, *Phys. Rev. B* **82**, 054415 (2010).
- ⁵⁷ A. Ohtomo and H. Y. Hwang, *Nature* **427**, 423 (2004).
- ⁵⁸ J. Lee and A. A. Demkov, *Phys. Rev. B* **78**, 193104 (2008).
- ⁵⁹ J. Kanamori, *Journal of Physics and Chemistry of Solids* **10**, 87 (1959).

- ⁶⁰ L. Sun, Y.-W. Fang, J. He, Y. Zhang, R. Qi, Q. He, R. Huang, P. Xiang, X.-D. Tang, P. Yang, J. Chu, Y.-H. Chu, and C.-G. Duan, *J. Mater. Chem. C* **5**, 5494 (2017).
- ⁶¹ C. Zener, *Phys. Rev.* **82**, 403 (1951).
- ⁶² J. Jilili, F. Cossu, and U. Schwingenschlögl, *Sci Rep* **5**, 1371 (2015).
- ⁶³ Y.-W. Fang, “[Dataset] First-principles design of ferromagnetic monolayer MnO₂ at the complex interface,” Zenodo: 10.5281/zenodo.7847492 (2023).